



Article

# Characterization of Hyaluronic Acid-Coated PLGA Nanoparticles by Surface-Enhanced Raman Spectroscopy

Giuseppe La Verde <sup>1</sup>, Antonio Sasso <sup>2,\*</sup>, Giulia Rusciano <sup>2</sup>, Angela Capaccio <sup>2</sup>, Sabato Fusco <sup>3</sup>, Laura Mayol <sup>4</sup>, Marco Biondi <sup>1</sup>, Teresa Silvestri <sup>5</sup>, Paolo A. Netti <sup>6,7,8</sup>, Marco La Commara <sup>1</sup>, Valeria Panzetta <sup>6,7,8</sup> and Mariagabriella Pugliese <sup>2</sup>

<sup>1</sup> Department of Pharmacy, University of Naples Federico II, Via Domenico Montesano, 80131 Naples, Italy

<sup>2</sup> Department of Physics "E. Pancini", University of Naples Federico II, Via Cinthia, 80126 Naples, Italy

<sup>3</sup> Department of Medicine and Health Sciences "V. Tiberio", University of Molise, Via Cesare Gazzani, 86100 Campobasso, Italy

<sup>4</sup> Department of Advanced Biomedical Sciences, University of Naples Federico II, Via Pansini, 80131 Naples, Italy

<sup>5</sup> Laboratory of Nanotechnology for Precision Medicine, Italian Institute of Technology, Via Morego, 16163 Genoa, Italy

<sup>6</sup> Department of Chemical, Materials and Production Engineering, University of Naples Federico II, Piazzale Vincenzo Tecchio, 80125 Naples, Italy

<sup>7</sup> Interdisciplinary Research Centre on Biomaterials CRIB, University of Naples Federico II, Piazzale Vincenzo Tecchio, 80125 Naples, Italy

<sup>8</sup> Center for Advanced Biomaterials for Healthcare @CRIB, Italian Institute of Technology, Largo Barsanti e Matteucci 53, 80125 Naples, Italy

\* Correspondence: antonio.sasso@unina.it

**Abstract:** Nanoparticles (NPs) coated with hyaluronic acid (HA) seem to be increasingly promising for targeted therapy due to HA chemical versatility, which allows them to bind drugs of different natures, and their affinity with the transmembrane receptor CD-44, overexpressed in tumor cells. However, an essential aspect for clinical use of NPs is formulation stability over time. For these reasons, analytical techniques capable of characterizing their physico-chemical properties are needed. In this work, poly(lactide-co-glycolide) (PLGA) NPs with an average diameter of 100–150 nm, coated with a few 10 s of nm of HA, were synthesized. For stability characterization, two complementary investigative techniques were used: Dynamic Light Scattering (DLS) and Surface-Enhanced Raman Scattering (SERS) spectroscopy. The first technique provided information on size, polydispersity index, and zeta-potential, and the second provided a deeper insight on the NP surface chemicals, allowing distinguishing of HA-coated NPs from uncoated ones. Furthermore, in order to estimate formulation stability over time, NPs were measured and monitored for two weeks. SERS results showed a progressive decrease in the signal associated with HA, which, however, is not detectable by the DLS measurements.

**Keywords:** nanoparticles; hyaluronic acid; Raman spectroscopy; SERS; stability characterization



**Citation:** La Verde, G.; Sasso, A.; Rusciano, G.; Capaccio, A.; Fusco, S.; Mayol, L.; Biondi, M.; Silvestri, T.; Netti, P.A.; La Commara, M.; et al. Characterization of Hyaluronic Acid-Coated PLGA Nanoparticles by Surface-Enhanced Raman Spectroscopy. *Int. J. Mol. Sci.* **2023**, *24*, 601. <https://doi.org/10.3390/ijms24010601>

Academic Editor: Diego Guidolin

Received: 23 November 2022

Revised: 17 December 2022

Accepted: 25 December 2022

Published: 29 December 2022



**Copyright:** © 2022 by the authors. Licensee MDPI, Basel, Switzerland. This article is an open access article distributed under the terms and conditions of the Creative Commons Attribution (CC BY) license (<https://creativecommons.org/licenses/by/4.0/>).

## 1. Introduction

Traditional chemotherapy treatments, while being the gold standard in cancer treatment, present challenges for patient effects, such as inhibition of fast-turnover healthy cells (hair follicles, bone marrow, and gastrointestinal cells) [1], and multidrug resistance (MDR), typical of the most aggressive tumors [2]. To mitigate these adverse effects, in recent years, alternative approaches, usually going by the name of nanomedicine, have been developing.

This branch of medicine is producing promising results in diagnosis, imaging, drug administration, and therapy practices [3]. The strategy adopted involves the use of nanoparticles (NPs), of various natures, with diameters 1–100 nm [4]. NPs have, in fact, the potential

to improve pharmacokinetics, stability, solubility, half-life, and accumulation in the target sites of chemotherapeutic drugs and, therefore, to enhance their therapeutic index compared to conventional therapy [5].

Nowadays, nanomedicine is starting to propose the use of NPs in combination with other cancer therapies, such as immunotherapy, hyperthermia, and radiotherapy. For example, NPs have been used as radiosensitizers which increase radiation damage to tumors [6] or, vice versa, the effects of ionizing radiation on cancer cell morphology and on the expression of surface-adhesion molecules [7,8] have been exploited to promote the cellular internalization of NPs [9,10].

Particle size, along with surface composition, plays a crucial role for drug delivery. NPs with dimensions below 200 nm are not detected by the mononuclear phagocytic system, and therefore they can remain in circulation longer [11], but at the same time, they can be directly eliminated by the renal system. Clearly, by optimizing the carrier size it is possible to promote passive penetration, for example by enhanced permeability and retention (EPR) effect [12]. In addition, NP functionalization can exploit active recognition mechanisms or can allow the crossing of a low-permeability barrier, such as the blood–brain barrier) transporting the drug to a target organ [13].

Among the molecules used to promote NP uptake, hyaluronic acid (HA) plays a major role for its tropism toward the cluster determinant 44 (CD-44), which is overexpressed in a wide array of malignant tumors [14–16], and is therefore attractive for the formulation of NPs for active tumor targeting [17,18].

In this *scenario*, it is crucial to prepare a stable formulation that guarantees the safety and efficacy of the pharmaceutical compounds. Critical points involve all steps of the process from synthesis to transport and storage. Although both physical and chemical alteration processes are known, ensuring the stability of a formulation remains a complex problem that is not yet easy to manage [19].

The aim of this work is to prepare HA-coated NPs and investigate their surface characteristics by combining complementary techniques. In particular, NPs were produced through the nanoprecipitation technique [20] using HA with a mean molecular weight of 800 kDa, which maximizes NP internalization in tumor cells [21]. To study the formulation stability, two different techniques were used: Dynamic Light Scattering (DLS) and Surface-Enhanced Raman Scattering (SERS) spectroscopy. DLS represents one of the most used techniques to monitor physico-chemical parameters of NPs; nevertheless, it does not provide information on the chemical nature of possible variation in these parameters. For example, for HA-coated NPs, the increase in mean diameter over time remains difficult to interpret; it could be ascribed to both the alteration of the tertiary structure of the HA or to the aggregation of HA debris in the solution [22–24].

Raman Spectroscopy (RS) is a well-established label-free technique with high chemical specificity (finger-printing character) [25]. However, being based on inelastic scattering, its cross-section is rather low ( $10\text{--}30\text{ cm}^2$ ), limiting its application to cases where high sensitivity is not required. This drawback has been overcome in recent decades by a variant of it, Surface-Enhanced Raman Spectroscopy (SERS), based on localized surface plasmon resonances (LSPR) which occur in metallic nanostructures (mainly Au and Ag) irradiated by laser radiation of a suitable wavelength. In particular, a huge amplification of the laser field (of typically between six and eight orders of magnitude) originates in the gaps which are formed in these nanostructures (hot-spots). This allows the detection of analytes at very low concentrations, down to the single-molecule regime. In addition, since the SERS amplification decreases rapidly (within a few tens of nm) moving away from the metal surface, the technique is particularly suitable for the study of interfaces, since the bulk contribution becomes negligible with respect to the interface placed in the proximity of the SERS substrate.

The SERS technique has been used in a very large number of applications in the fields of materials, chemistry, and biology [26–29]. For example, our group has analyzed the spore coat formation in *Bacillus subtilis* using both SERS [30] and Tip-Enhanced Raman

Scattering (TERS) techniques [31]. However, according to our knowledge, few studies have been dedicated to the characterization of composite NPs and, in particular, to their external surface.

The novelty proposed in this work is to study the structure of HA-coated NPs composed by a core and a thin outer layer. SERS is particularly suitable for this type of investigation because it combines the high sensitivity required to detect and discriminate the external thin HA layer from the rest of the NP. More specifically, we demonstrate that the SERS technique allows distinguishing of HA-coated from uncoated NPs. In addition, by following over the time the evolution of the signal intensity corresponding to HA, we also studied HA-coating degeneration (aging). This approach holds promise for a reliable characterization of the external shell of newly developed NPs for biomedical and biotechnological applications.

## 2. Results and Discussion

### 2.1. DLS Measurements

Two different types of formulations were prepared by nanoprecipitation technique: control NPs, consisting of an organic blend of poly (lactide-co-glycolide, PLGA) and poloxamers, (F68 and F127) and HA-decorated NPs, hereinafter indicated as PP-NPs and HA-PP-NPs, respectively.

In order to evaluate the stability over time of PP-NPs and HA-PP-NPs stored at 4 °C DLS measurements were carried out at room temperature and at three different time points, 0, 7, and 14 days ( $T_0$ ,  $T_7$ ,  $T_{14}$ ). Mean diameter, PDI, and  $\zeta$ -potential found for these times are reported in Table 1.

At the first time point ( $T_0$ ), PP-NPs exhibited a mean diameter of about 100 nm and negative  $\zeta$ -potential of  $-26$  mV. In the case of HA-PP-NPs, the significant enhancement of their mean diameter of about 30% (Kruskal–Wallis test,  $p < 0.001$ ) and the significant reduction in their  $\zeta$ -potential up to  $-34$  mV (Kruskal–Wallis test,  $p < 0.01$ ) indicate a successful external decoration with HA [32].

**Table 1.** DLS measurements at  $T_0$ ,  $T_7$ , and  $T_{14}$ .

Formulation	Mean Diameter (nm)	PDI	$\zeta$ (mV)	Time
PP-NPs	109 ± 11	0.11 ± 0.04	$-26 \pm 6$	$T_0$
HA-PP-NPs	145 ± 16	0.14 ± 0.076	$-34 \pm 8$	
PP-NPs	118 ± 15	0.13 ± 0.05	$-26 \pm 5$	$T_7$
HA-PP-NPs	135 ± 23	0.15 ± 0.05	$-24 \pm 4$	
PP-NPs	117 ± 10	0.16 ± 0.05	$-23 \pm 2$	$T_{14}$
HA-PP-NPs	142 ± 17	0.13 ± 0.06	$-29 \pm 4$	

Dimensional stability was established by evaluating the hydrodynamic diameter in water, up to  $T_{14}$ . Both NPs were stable up to  $T_{14}$  and no phenomenon of self-aggregation was observed.

On the contrary, the enhancement of  $\zeta$ -potential for HA-PP-NP formulation already at  $T_7$  (Kruskal–Wallis test,  $p < 0.001$ ) and for PP-NPs at  $T_{14}$  (Kruskal–Wallis test,  $p < 0.005$ ) indicated a likely alteration of the NP surface that could be ascribed to poloxamers and HA (the two layers most exposed and therefore susceptible to changes in PP-NPs and HA-PP-NPs, respectively). It must also be specified that  $\zeta$ -potential changes in the time frame of the observation can be reasonably ascribed to statistical fluctuations in the measurement.

To obtain direct information on the physico-chemical structure of the NPs, a spectroscopic technique was employed to monitor the evolution of the external regions of NP.

## 2.2. Spontaneous Raman Spectroscopy of Bulk Materials

Preliminary SR measurements were carried out on the single components forming NPs, i.e., PLGA, F127, F68, and HA, in order to know their main spectroscopic features.

Measurements of all these chemical species were performed using samples in the form of powder. Figure 1 shows the averaged Raman spectra of the main components in the 300–3900  $\text{cm}^{-1}$  spectral range, acquired with a laser power of 15 mW and an integration time of 50 s. Since the Raman spectrum of F127 is quite similar to F68, as will be explained later, for sake of simplicity it is not plotted herein.

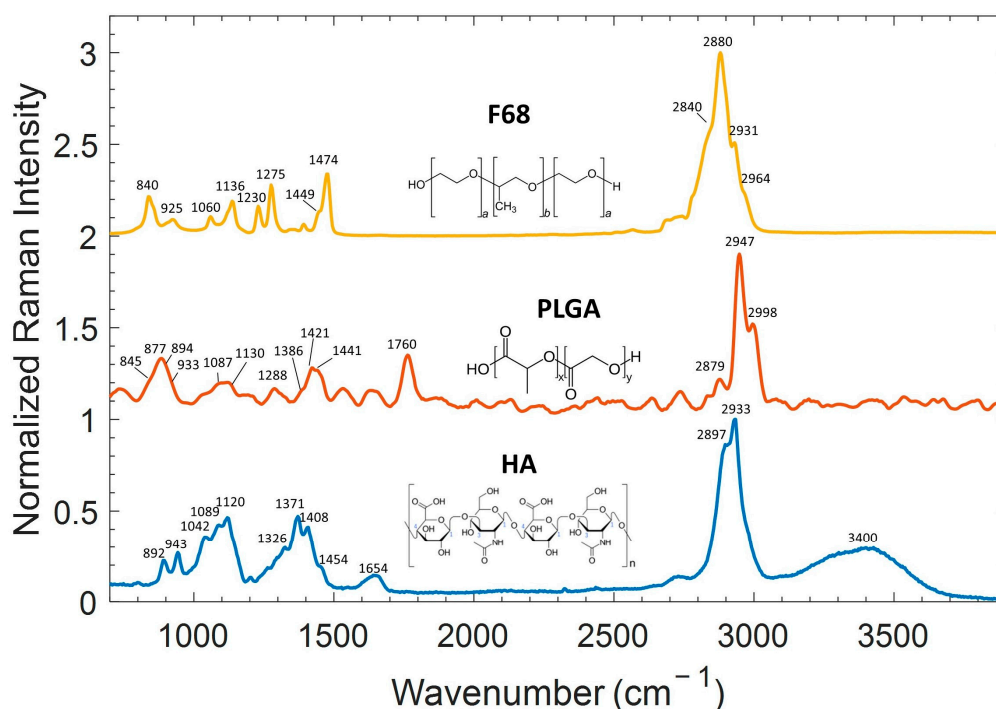


**Figure 1.** Comparison of Raman spectra of (yellow) F68 ( $a = 76$ ,  $b = 29$ ), (red) PLGA ( $x = 50$ ,  $y = 50$ ), and (blue) HA powders acquired with an integration time of 50 s and a Raman probe of 15 mW. For a better comparison, spectra were normalized and shifted.

Following the literature concerning HA Raman studies [22,33–35], the main bands could be assigned. The relatively narrow bands at  $\sim 892 \text{ cm}^{-1}$  and  $\sim 943 \text{ cm}^{-1}$  are ascribed to  $\beta$ -linkages and C-C stretching modes, while the broad bands around  $1000 \text{ cm}^{-1}$  derive from the overlapping of the C-C and C-O stretching modes ( $\sim 1042 \text{ cm}^{-1}$ ), C-OH bending mode of an acetyl group ( $\sim 1089 \text{ cm}^{-1}$ ), and C-OH and C-H bending modes ( $\sim 1120 \text{ cm}^{-1}$ ). The other wide band around  $1400 \text{ cm}^{-1}$  also results from the superposition of several vibrational modes: an amide III band at  $\sim 1326 \text{ cm}^{-1}$ , and asymmetric and symmetric  $\text{CH}_3$  bending vibrational modes at  $\sim 1371 \text{ cm}^{-1}$  and  $\sim 1454 \text{ cm}^{-1}$ , respectively. The bands at  $\sim 1408 \text{ cm}^{-1}$  result from CH deformation and the symmetric  $\text{COO}^-$  stretching mode which is a vibration sensitive to hydrogen bonding, while the band at  $\sim 1654 \text{ cm}^{-1}$  is ascribed to C=C and amide I C=O vibrations, with low-frequency shoulders deriving from asymmetric  $\text{COO}^-$  stretching vibrational modes. Finally, the bands at  $2897$  and  $2933 \text{ cm}^{-1}$  correspond to the C-H and NH stretching modes. In addition, the band around  $3400 \text{ cm}^{-1}$  is ascribed to the OH-free mode and to symmetrical and asymmetrical OH stretching modes.

In the case of PLGA, based on previous works [36,37], the peaks detected are ascribable to vibrational modes of lactic (LA) or/and glycolic (GA) units. PLGA is a copolymer formed by the two units: poly(D,L-lactide) (PLA) and poly(glycolide) (PGA) polymers. As a matter of fact, the spectra of PLGA shows some differences from the spectra of single units due of the interaction of the two polymers. In particular, the main interesting features are the

1760  $\text{cm}^{-1}$  band assigned to C=O stretching of the ester groups and the stretching modes of the  $\text{CH}_3$  (LA) and  $\text{CH}_2$  (GA) groups at 2998 and 2947  $\text{cm}^{-1}$ , respectively.

Regarding the Raman spectrum of F68 [38], the assignments of the main vibrational modes are listed in Table 2. The F68 is a poloxamer, i.e., a triblock copolymer composed of a central hydrophobic chain of polyoxypropylene (PPO) linked to two hydrophilic chains of polyoxyethylene (PEO). The relative intensities of several peaks in Raman spectrum are dependent on the PPO/PEO ratio and the conformation of the copolymer. In this case, both F68 and F127 are characterized by a low ratio of PPO/PEO, corresponding to 0.19 and 0.32, respectively. For this reason, Raman spectra are mostly due to PEO unit contribution, which gives rise to the most prominent bands centered at 840  $\text{cm}^{-1}$  ( $\rho(\text{CH}_2)$ ), 1136  $\text{cm}^{-1}$  ( $\nu(\text{CH}_2)$ ),  $\nu(\text{CC})$ , 1275  $\text{cm}^{-1}$  ( $\delta(\text{CH})$ ), 1474  $\text{cm}^{-1}$  ( $\text{CH}_2$  scissoring), and 2880  $\text{cm}^{-1}$  ( $\nu(\text{CH}_2)$ ) [39].

**Table 2.** Raman assignments of F68, PLGA, and HA ( $\nu$  = stretching,  $\rho$  = rocking,  $\delta$  = bending,  $\tau$  = twist).

F68	PLGA	HA	Tentative Assignment ( $\text{cm}^{-1}$ )
840	845 877 894		$\rho\text{CH}_2$ $\nu\text{C-COO}$ $\rho\text{CH}_2, \nu\text{C-C}$
		892	$\beta$ -linkages
925	933		$\rho\text{CH}_2$ $\rho\text{CH}_2, \nu\text{C-C}$
		943	$\nu\text{C-C}, \nu\text{C-O-C}$
		1042	$\nu\text{C-C}, \nu\text{C-O}$
1060	1087	1089	$\rho\text{CH}_2, \nu\text{C-O}$
		1120	$\delta\text{C-OH}$
	1130		$\delta\text{C-OH}, \delta\text{CH}$
1136			$\rho\text{CH}_3$ asym
1230			$\nu\text{CH}_2, \nu\text{C-C}$
1275	1288		$\tau\text{CH}_2$ $\delta\text{CH}$
		1326	Amide III
	1386	1371	$\delta\text{CH}_3$ sym
		1408	$\delta\text{CH}, \delta\text{COO-}$
	1421		$\delta\text{CH}_2$
1449			$\text{CH}_2$ scissor
	1441	1454	$\delta\text{CH}_2, \delta\text{CH}_3$ asym
1474			$\text{CH}_2$ scissor
		1654	$\nu\text{C=C}, \text{Amide I C=O}$
	1760		$\nu\text{C=O}$
2840			$\nu\text{CH}_2$ sym
2880	2879		$\nu\text{CH}_2$ asym
		2897	$\nu\text{CH}$
		2933	$\nu\text{NH}$
2931			$\nu\text{CH}_3$ sym
	2947		$\nu\text{CH}_2$ sym
2964	2998		$\nu\text{CH}_3$ asym
		3200/3500	$\nu\text{OH}$

From the comparison of the Raman spectra of the three components, HA, PLGA, and F68, shown in Figure 1, a certain overlap between the bands is highlighted, especially for the vibrations involving  $\text{CH}_n$ .

The simultaneous presence of these three components, as occurs in HA-PP-NPs, makes spectra analysis difficult, as will be discussed later.

### 2.3. SERS and Raman Analysis of HA

As already mentioned, the SERS technique allows the detection of chemical species at low concentration, preserving the fingerprinting character of Raman spectroscopy. In

Figure 2, the SR of a solid HA sample, discussed in the previous paragraph, and the average SERS spectrum of HA solution at the concentration of 2.5 mg/mL are compared.

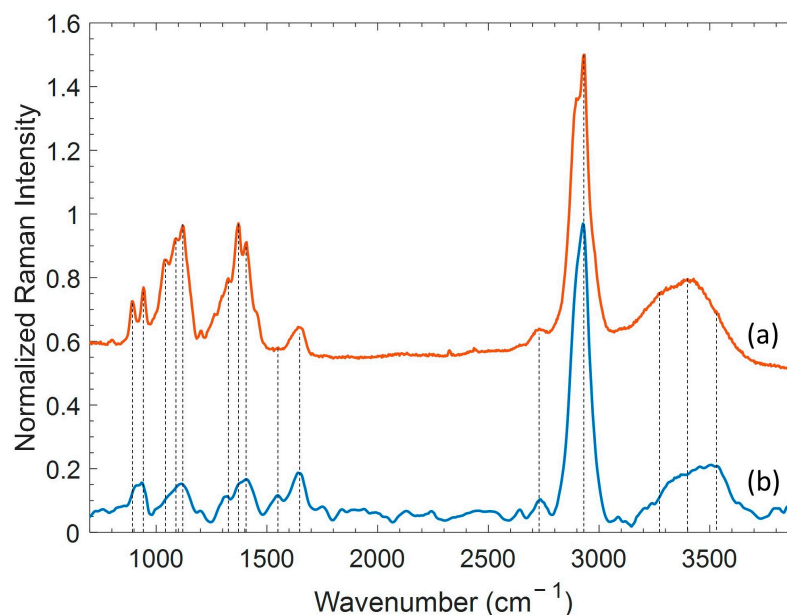


**Figure 2.** Comparison of Raman spectrum of HA powder (a) and SERS spectrum of HA solution (b). The spectra were normalized and shifted.

The SERS measurements were performed by placing a volume of 20  $\mu\text{L}$  of solution upon the SERS substrate, allowing solvent evaporation. The evaporated droplet left on the surface a spot with a diameter of about 5 mm. After that, a map of 100 points (spectra) in an area of  $25 \times 25 \mu\text{m}^2$  was collected four times, in four corresponding different points of the dried droplet ( $p = 300 \mu\text{W}$ ,  $\tau = 1 \text{ s}$ ). By averaging the acquired SERS spectra, possible SERS intensity variability due to the inhomogeneous distribution of molecules on the surface (coffee-ring effect [40]) was minimized.

By comparing the Raman and SERS spectra reported in Figure 2, it can be appreciated that both the bandwidth and the relative intensity of the bands show some differences. The broadening of the peaks reflects the order character of the sample: the narrower the peak, the more ordered the structure is. Thus, the SERS spectrum of HA dissolved in solution shows broader bands, probably because of the random orientation of the molecules over the metal surface. In addition, due to the surface selection rule for SERS [41], vibrational modes can be amplified or depressed according to if polarizability changes normally or parallel to the surface.

#### 2.4. SERS of PP-NPs and HA-PP-NPs

We analyzed HA-PP-NPs samples at a density of about  $8 \times 10^{11}$  particles/mL, estimated from DLS measurements. Therefore, by using SR this means that in the detection volume  $V_{\text{det}} = \pi w^2 \times h_{\text{eff}} = 2.3 \mu\text{m}^3$  are present in average  $\sim 2$  particles, a too-low number of particles compared to the sensitivity of SR. Figure 3a, trace (i) shows the spectrum of HA solution acquired by SR with a power of 30 mW and a time integration of 50 s.

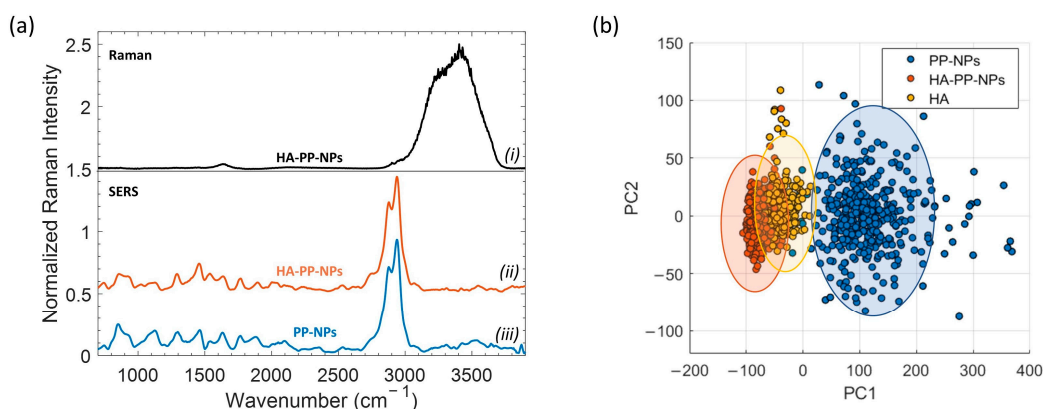


**Figure 3.** (a) Comparison of (i) Raman and SERS spectra of HA-PP-NP (ii) and PP-NP (iii) samples. The spectra were normalized and shifted; (b) score plot of PC1 versus PC2 for PP-NPs, HA-PP-NPs, and HA.

Except for a weak signal detectable in the region around  $\sim 2900\text{ cm}^{-1}$ , the only observed bands correspond to the bending and stretching mode of the water molecule at  $1640$  and  $3400\text{ cm}^{-1}$ , respectively. This proves that SR fails at the considered concentration. The Raman response is different when SERS is used: Figure 3a, traces (ii) and (iii), report the average SERS spectrum of HA-coated and uncoated NPs acquired after the evaporation of a  $20\text{ }\mu\text{L}$  droplet deposited upon a SERS substrate. It is also worth noting that the power used for SERS measurements was particularly low ( $P = 145\text{ }\mu\text{W}$ ) and the exposure time quite short ( $\tau = 2\text{ s}$ ) in order to avoid possible photo-thermal damage.

A careful comparison between the two SERS spectra shows significant differences. These mainly concern the bands around  $850\text{ cm}^{-1}$  and  $2750\text{ cm}^{-1}$ . These differences are better highlighted through the use of the principal component analysis (PCA) performed on the band at  $2750\text{ cm}^{-1}$  (see Figure 3b). For this analysis, we considered a number  $N = 400$  SERS spectra for each sample; a set of HA SERS spectra was also included as control. SERS spectra in the PCA space were projected according to the first two principal components. The score plot shows a clear difference between the two populations (PP-NPs and HA-PP-NPs) along PC1. Notably, the HA-PP-NP population tends to overlap with the set of spectra of HA. This result is consistent with the fact that HA-coated NPs expose this polymer to the SERS substrate and, hence, a certain similarity is expected between these two populations.

### 2.5. HA-PP-NP Aging SERS Analysis

In the previous section, we established that HA-PP-NPs can be chemically distinguished from PP-NPs by observing differences in their SERS spectra. Since HA is not covalently grafted to the NPs, it is to be expected that the stability of the particles is not durable over time. In fact, HA can be subjected to various processes that modify its consistency: it can simply be released and dispersed in the solution, or it can undergo a molecular rearrangement, such as swelling. In both cases, this can lead to an alteration of the Raman bands in terms of their intensities or frequency shifts. To investigate aging effects on HA-PP-NPs, SERS and DLS measurements were carried out in parallel and we adopted the following procedure. Once the HA-PP-NP sample was produced, we carried out a measurement campaign by taking a small aliquot of material from the mother solution, which was kept at a temperature of  $4\text{ }^{\circ}\text{C}$ . SERS measurements were performed depositing a droplet of volume  $20\text{ }\mu\text{L}$  on the SERS substrate, allowing it to dry in ambient air. For each sample, a series of 400 spectra was acquired over randomly selected points of the substrate. This protocol was applied to fresh sample (initial time  $T_0$ ) and repeated after one week ( $T_7$ ) and two weeks ( $T_{14}$ ). We observed macroscopic differences by comparing the average SERS spectra obtained at times,  $T_0$ ,  $T_7$ , and  $T_{14}$  in the spectral region between  $750$  and  $1000\text{ cm}^{-1}$ , as reported in Figure 4a. For complete comprehension, the average SERS spectrum of

PP-NPs at  $T_0$  was considered as reference. Following the Raman assignments of the HA spectrum discussed previously, the peak centered at  $892\text{ cm}^{-1}$  is clearly ascribed to the presence of HA on the surface of coated PP-NPs. Differently, the band at  $854\text{ cm}^{-1}$  is of no immediate assignment because it could be related to both PLGA and F68. Hence, more in general, this band could represent the contribution of the inner part of the NPs. In Figure 4a, the spectra have been normalized to the signal at  $854\text{ cm}^{-1}$ . A convenient way of showing this variation is reporting the ratio of the intensities of the two peaks,  $I_{892/854}$ , as a function of time (see Figure 4b). As we can see,  $I_{892/854}$  decreases by reaching approximately the value corresponding to PP-NPs. The fact that the behavior of HA-PP-NPs tends to that of naked PP-NPs suggests that HA is released over time, rather than subjected to some molecular reorganization with the rest of the nanoparticle core.

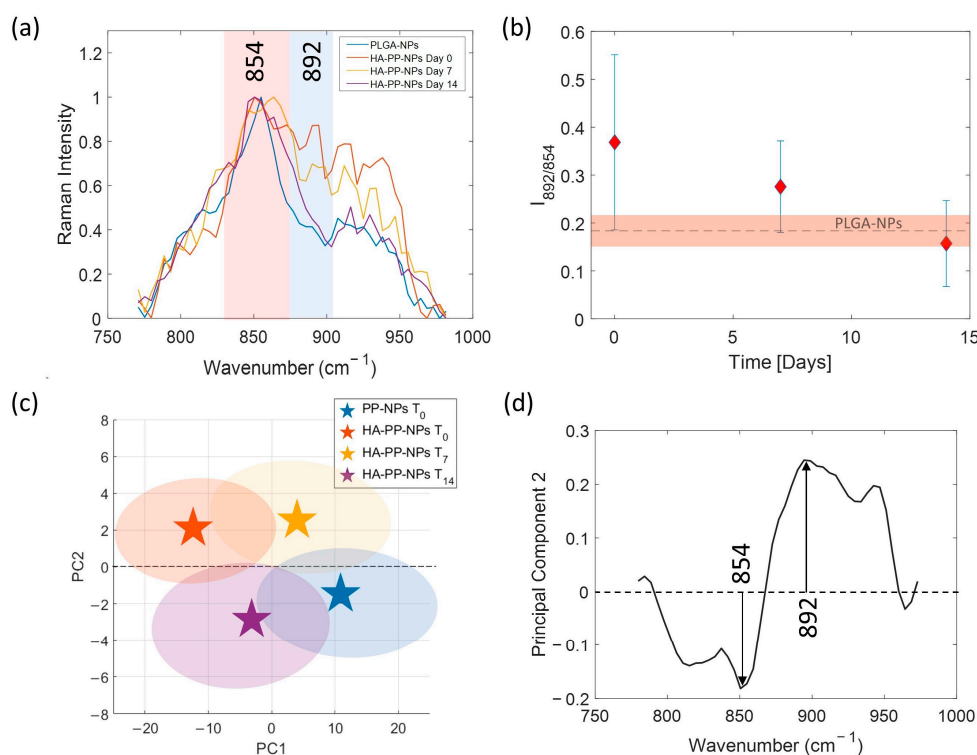


**Figure 4.** (a) Comparison of SERS spectra relative to PP-NPs  $T_0$  and HA-PP-NPs  $T_0$ ,  $T_7$ ,  $T_{14}$ ; (b) Plot of the ratio intensities  $I_{892/854}$  as a function of time. The ratio value relative to PP-NP  $T_0$  spectrum is reported as a dashed horizontal line and the corresponding error bar as a red box; (c) Score plot of PC1 versus PC2 for PP-NPs  $T_0$  and HA-PP-NPs  $T_0$ ,  $T_7$ ,  $T_{14}$ ; (d) Loading plot of PC2.

This claim is further confirmed by analyzing the four populations of SERS spectra, corresponding to the above-mentioned samples, with the PCA in the more significant spectral range  $750\text{--}1000\text{ cm}^{-1}$ . Figure 4c reports the outcomes of this analysis by showing the resulting cluster centroids of each group in the 2-D PCA score plot. At first glance, a net separation of the clusters distributed in PC space can be observed both along PC1 and PC2. Intriguingly, a clear interpretation of the differentiation along the second PC can be revealed by looking at the corresponding loading plot of PC2 reported in Figure 4d. The analysis of the loadings highlights an important inverse correlation between the peaks centered at  $854$  and  $892\text{ cm}^{-1}$ . The positive loading indicates that the groups lying along the positive direction of PC2, i.e., HA-PP-NPs at  $T_0$  and at  $T_7$ , are characterized by the presence in their SERS spectra of the spectral line centered at  $892\text{ cm}^{-1}$ , which is equivalent to the expression of the presence of the HA in these samples. On the contrary, the populations relative to PP-NPs at  $T_0$  and HA-PP-NPs at  $T_{14}$ , grouped along the negative direction of PC2, are characterized by spectral content of the peak at  $854\text{ cm}^{-1}$  which has a negative loading. This result reflects exactly the tendency observed in Figure 4b in which the intensity of the

peak relative to  $892\text{ cm}^{-1}$  of HA-PP-NPs reduces, approaching finally at  $T_{14}$  the same value of PP-NPs at  $T_0$  spectrum.

### 3. Materials and Methods

#### 3.1. NP Formulation

Poly (lactic-co-glycolic acid) (PLGA), lactide:glycolide 50:50, was obtained from Sigma-Aldrich (St. Louis, MO USA), while poloxamers (PEOa-PPOb-PEOa F127 (a = 100 and b = 65) and F68 (a = 76 and b = 29) were from Lutrol Lutrol Basf, Ludwigshafen, Germany. HA with a weight-average MW of 830 kDa was kindly provided by Altergon, Avellino, Italia.

Processes of NP formulation are schematized in Figure 5. NPs were prepared using the nanoprecipitation technique followed by solvent evaporation, as previously described [42]. Briefly, for both formulations (PP-NPs and HA-PP-NPs) an organic phase (O) made up of PLGA, F68, and F127 (mass ratio 1:0.5:0.5; overall polymer concentration was 1.5% *w/v*) in 5 mL of acetone was prepared. Subsequently, 640  $\mu\text{L}$  of ethanol (internal aqueous phase,  $W_0$ ) was added and  $W_0/O$  emulsion was obtained by sonication (3000 sonicator, Misonix, Farmingdale, NY, USA; 5 min, 4W, 419 microtip probe). The emulsion was added dropwise, through a syringe pump at a volumetric flow rate of 333.3  $\mu\text{L}/\text{min}$ , to 40 ml of an external aqueous phase (W) containing F68 and F127 (0.0375 *w/v* each). In the case of HA-PP-NPs, 30 mg of HA 830 kDa was added to the W phase. Subsequently, acetone was evaporated for about 4 h under magnetic stirring. The resulting NP suspension was divided into 2 mL tubes and centrifuged three times (Hettich Zentrifugen, Tuttlingen Germany; 10,000 rpm, 10 min). After the first two centrifuges, 1 mL of supernatant was discarded and replaced with an equal volume of double-distilled water. After the last centrifuge, 1.5 mL of supernatant was removed, and 0.5 mL of PBS (sodium chloride, potassium chloride, and disodium phosphate) was added. The obtained formulation was filtered with 0.2  $\mu\text{m}$  filters and stored at 4  $^{\circ}\text{C}$ .

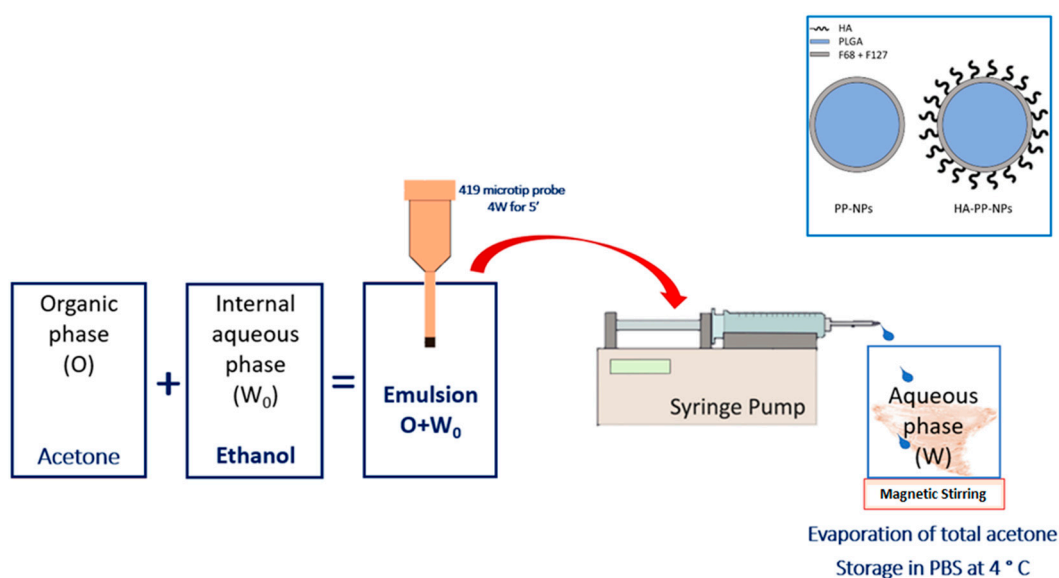


**Figure 5.** Schematization of NP formulation process with the nanoprecipitation technique. The inset in the upper right corner shows the two possible formulations.

#### 3.2. Dynamic Light Scattering

Dynamic Light Scattering (DLS) is the most used technique to analyze particles at nanoscale. The DLS technique is based on scattering due to a laser beam that strikes a

colloidal suspension. Therefore, the size of the particles can be extrapolated from analysis of the fluctuations in the intensity of the scattered light using the Stokes–Einstein equation:

$$D = (k_B T) / (6\pi\eta R_H), \quad (1)$$

where  $D$  is the translational diffusion coefficient,  $k_B$  is the Boltzmann constant,  $T$  is the absolute temperature,  $\eta$  is the viscosity coefficient of the solvent, and  $R_H$  is the hydrodynamic radius. The NP solutions were stored at 4 °C for 14 days. Then, mean diameter and PDI of NPs were obtained through DLS measurements by laser light scattering (Zetasizer Nano ZS, Malvern Instruments, Malvern, UK) at room temperature on NP suspensions in ultra-water at 0.1 mg/mL at three different time points (0, 7, and 14 days). Twelve runs were run for each sample.

In addition, through the electrophoretic mobility, the zeta-potential can also be estimated [43]. If the  $\zeta$  value is high, electrostatic repulsion prevents the aggregation of the dispersed particles, while when it is low the attractive forces prevail, and the species give rise to coagulation phenomena. Negative values between  $-20$  and  $-40$  mV correspond to particles that are unlikely to aggregate, are stable, non-toxic, and have a high penetration capacity. Positive  $\zeta$  values are associated with particles usually toxic and potentially fusogenic with cells [44,45].

### 3.3. Raman Analysis

Raman and SERS measurements were performed using a commercial system (WiTec, mod Alpha300 RA) equipped with a frequency-doubled Nd/YAG laser emitting at 532 nm a maximum power of 30 mW. The laser beam was focused with a 20× objective lens. Scattered photons were collected in a back-scattering geometry through the same focusing objective lens. Inelastic photons were separated from elastic photons using an edge-filter and sent via a 100  $\mu\text{m}$  core fiber to a high-throughput spectrometer. Spectra were acquired with a thermoelectrically cooled CCD camera ( $T = -60$  °C).

### 3.4. SERS Substrates

Details on the procedure used for the fabrication of SERS substrates are reported in [46]. Briefly, a Ag film of 30 nm was deposited on a Cr/Au bilayer (3 nm Cr, 10 nm Au), preliminarily deposited on a  $15 \times 15 \text{ mm}^2$  glass coverslip in order to optimize the Ag adhesion. Depositions were performed using a magnetron sputtering system (Q300T D Plus, Quorum Tech., Lewes, England). The so-produced films were rather flat, with an average roughness of about 2 nm. In order to induce a nanostructuring of the Ag film (necessary to make the films SERS-active), a cold plasma treatment was applied to them for 90 s by using an inductively coupled plasma system (PDC-32G-2, Harrick Plasma, Ithaca, NY, USA) in a synthetic air atmosphere. This operation led to a coral-like porous nanostructured surface. Nevertheless, the presence of oxygen in the discharge, essential to sustain the nano-structuration mechanisms of the surface, creates a thin layer of Ag-oxide with consequent loss of plasmonic properties. The metallic character of the pristine surface, without altering its nanostructured pattern, was restored through a further 50 s of plasma treatment in an Ar atmosphere [47]. In Figure 6, an image of our substrate obtained with scanning electronic microscopy (SEM) is shown.

The SERS substrates so-produced were characterized using 4-MBA as a probe molecule. Interesting performances in terms of enhancement factor (average  $EF \sim 10^7$ ) and spatial reproducibility were obtained.

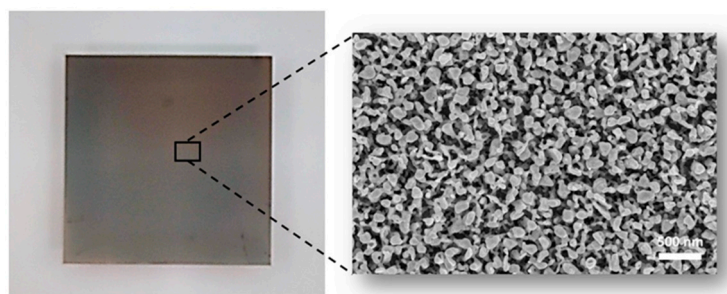


**Figure 6.** Digital photograph of SERS substrate fabricated on a  $15 \times 15 \text{ mm}^2$  glass coverslip and SEM image of the nanostructured Ag film, exhibiting the typical coral-like morphology.

### 3.5. Statistical Analysis of DLS

Descriptive statistics of DLS data (mean diameter, PDI, and  $\zeta$ -potential) consisted of mean values and standard deviation. The normality of data was checked by the Shapiro–Wilk test ( $p$  values  $< 0.05$  indicates non-normal distribution). Statistical comparisons were performed with a Student’s unpaired test when data exhibit a normal distribution. Otherwise, a nonparametric Kruskal–Wallis test was used. Differences were considered significant for  $p$  values less than 0.05.

### 3.6. Statistical Analysis of SERS Spectra

PCA is a well-known multivariate statistical tool suitable to analyze multidimensional datasets. Its basic principle consists of an orthogonal linear transformation of the initial dataset (SERS spectra in our case) into a new coordinate system such that the greatest variance in the projected data comes to lie on the new coordinates. The first coordinate, called the first principal component (PC1), explains the maximum variance in the dataset; the following components consider the residual variance, and so on. Each PC is composed of scores and loadings: the scores represent the variance on sample direction, hence being used to highlight similarities/dissimilarities between samples; the loadings represent the variance on wavenumber direction, being used to identify possible spectral features responsible for cluster differentiation. Therefore, PCA allows condensation of the score plot, the acquired spectra in a set of points having as coordinates the respective PC $_i$ ,  $i = 1, 2, \dots, n$ . The affinity between spectra referring to different samples appears from the degree of clustering of the points in the PC space. In this experiment, SERS spectra were pre-treated by using a custom-made routine developed in order to eliminate spurious cosmic ray contributions and to subtract a fourth-order polynomial background contribution.

## 4. Conclusions

This work confirms the need to combine the more common DLS technique with the SERS technique to characterize the physico-chemical properties of HA-coated and uncoated NPs. In particular, the information obtainable from the DLS, such as dimensions, polydispersion index, and zeta-potential, are not able by themselves to fully describe the nature of the external coating of the NPs and their evolution over time. In this regard, the literature has not yet shed full light. In our study, the SERS technique was chosen for its high chemical specificity, its high sensitivity, and for the sub-diffraction resolution along the direction normal to the SERS substrate. All these features were precious for detecting the thin HA layer around the PP NPs, distinguishing it from the rest of the core NPs. This allowed us to clearly distinguish HA-coated from uncoated NPs. Even more interesting, SERS allows monitoring of the time evolution of the surface chemistry of the NPs, obtaining information about their stability. In this experiment, the DLS results show that, over two weeks, particle sizes do not have a significant tendency to change. On the other hand, zeta-potential unequivocally shows the tendency of NPs to be less charged. Similarly, by analyzing the SERS spectra, it is observed that, in the same time period, the intensity of the

vibrational band  $892\text{ cm}^{-1}$ , associated with HA, tends to decrease compared to at  $854\text{ cm}^{-1}$ , probably corresponding to PLGA or to poloxamer.

These results offer further opportunities, for example, to optimize the NP synthesis procedure to make NPs as stable as possible over time and to integrate different analysis techniques to obtain more detailed information.

**Author Contributions:** Conceptualization: G.L.V., M.P., V.P.; resources: A.S., L.M., M.B., P.A.N.; investigation: G.L.V., A.C., G.R.; data curation: G.L.V., V.P., A.C.; formal analysis: G.L.V., V.P., A.S., A.C., G.R.; writing—original draft: G.L.V., A.S., A.C., G.R.; visualization: M.P., A.S.; writing—review and editing: G.L.V., A.S., G.R., A.C., L.M., M.B., T.S., S.F., M.L.C., P.A.N., V.P., M.P.; supervision and funding acquisition: M.P. All authors have read and agreed to the published version of the manuscript.

**Funding:** This research received no external funding.

**Institutional Review Board Statement:** Not applicable.

**Informed Consent Statement:** Not applicable.

**Data Availability Statement:** Data are contained within the article.

**Conflicts of Interest:** The authors declare no conflict of interest.

## References

1. Zraik, I.M.; Heß-Busch, Y. Management of chemotherapy side effects and their long-term sequelae. *Urologe A* **2021**, *60*, 862–871. [[CrossRef](#)] [[PubMed](#)]
2. Baguley, B.C. Multidrug resistance in cancer. *Methods Mol. Biol.* **2010**, *596*, 1–14. [[CrossRef](#)] [[PubMed](#)]
3. Avitabile, E.; Bedognetti, D.; Ciofani, G.; Bianco, A.; Delogu, L.G. How can nanotechnology help the fight against breast cancer? *Nanoscale* **2018**, *10*, 11719–11731. [[CrossRef](#)]
4. Strambeanu, N.; Demetrovici, L.; Dragos, D.; Lungu, M. Nanoparticles: Definition, Classification and General Physical Properties. In *Nanoparticles' Promises and Risks*; Lungu, M., Neculae, A., Bunoiu, M., Biris, C., Eds.; Springer: Cham, Switzerland, 2015. [[CrossRef](#)]
5. Shi, J.; Kantoff, P.W.; Wooster, R.; Farokhzad, O.C. Cancer nanomedicine: Progress, challenges and opportunities. *Nat. Rev. Cancer* **2017**, *17*, 20–37. [[CrossRef](#)] [[PubMed](#)]
6. Su, X.Y.; Liu, P.D.; Wu, H.; Gu, N. Enhancement of radiosensitization by metal-based nanoparticles in cancer radiation therapy. *Cancer Biol. Med.* **2014**, *11*, 86–91. [[CrossRef](#)] [[PubMed](#)]
7. Panzetta, V.; La Verde, G.; Pugliese, M.; Artiola, V.; Arrichiello, C.; Muto, P.; La Commara, M.; Netti, P.A.; Fusco, S. Adhesion and migration response to radiation therapy of mammary epithelial and adenocarcinoma cells interacting with different stiffness substrates. *Cancers* **2020**, *12*, 1170. [[CrossRef](#)]
8. La Verde, G.; Artiola, V.; Panzetta, V.; Pugliese, M.; Netti, P.A.; Fusco, S. Cytoskeleton Response to Ionizing Radiation: A Brief Review on Adhesion and Migration Effects. *Biomedicines* **2021**, *9*, 1102. [[CrossRef](#)]
9. Davies, C.d.L.; Lundström, L.M.; Frengen, J.; Eikenes, L.; Bruland, Ø.S.; Kaalhus, O.; Hjelstuen, M.H.; Brekken, C. Radiation improves the distribution and uptake of liposomal doxorubicin (caelyx) in human osteosarcoma xenografts. *Cancer Res.* **2004**, *64*, 547–553. [[CrossRef](#)]
10. Panzetta, V.; Pugliese, M.; di Gennaro, G.; Federico, C.; Arrichiello, C.; Muto, P.; Netti, P.A.; Fusco, S. X-rays affect cytoskeleton assembly and nanoparticle uptake: Preliminary results. *Il Nuovo Cim.* **2018**, *41*, 204. [[CrossRef](#)]
11. Owens, D.E., 3rd; Peppas, N.A. Opsonization, biodistribution, and pharmacokinetics of polymeric nanoparticles. *Int. J. Pharm.* **2006**, *307*, 93–102. [[CrossRef](#)]
12. Yetisgin, A.A.; Cetinel, S.; Zuvin, M.; Kosar, A.; Kutlu, O. Therapeutic nanoparticles and their targeted delivery applications. *Molecules* **2020**, *25*, 2193. [[CrossRef](#)] [[PubMed](#)]
13. Guarnieri, D.; Muscetti, O.; Falanga, A.; Fusco, S.; Belli, V.; Perillo, E.; Battista, E.; Panzetta, V.; Galdiero, S.; Netti, P.A. Surface decoration with gH625-membranotropic peptides as a method to escape the endo-lysosomal compartment and reduce nanoparticle toxicity. *Nanotechnology* **2015**, *26*, 415101. [[CrossRef](#)] [[PubMed](#)]
14. Ponta, H.; Sherman, L.; Herrlich, P.A. CD44: From adhesion molecules to signalling regulators. *Nat. Rev. Mol. Cell Biol.* **2003**, *4*, 33–45. [[CrossRef](#)] [[PubMed](#)]
15. Naor, D.; Sionov, R.V.; Ish-Shalom, D. CD44: Structure, function, and association with the malignant process. *Adv. Cancer Res.* **1997**, *71*, 241–319. [[CrossRef](#)]
16. Yan, Y.; Zuo, X.; Wei, D. Concise Review: Emerging Role of CD44 in Cancer Stem Cells: A Promising Biomarker and Therapeutic Target. *Stem Cells Transl. Med.* **2015**, *4*, 1033–1043. [[CrossRef](#)]
17. Fallacara, A.; Baldini, E.; Manfredini, S.; Vertuani, S. Hyaluronic Acid in the Third Millennium. *Polymers* **2018**, *10*, 701. [[CrossRef](#)]

18. Hou, X.; Zhong, D.; Chen, H.; Gu, Z.; Gong, Q.; Ma, X.; Zhang, H.; Zhu, H.; Luo, K. Recent advances in hyaluronic acid-based nanomedicines: Preparation and application in cancer therapy. *Carbohydr. Polym.* **2022**, *292*, 119662. [[CrossRef](#)]
19. Wu, L.; Zhang, J.; Watanabe, W. Physical and chemical stability of drug nanoparticles. *Adv. Drug Deliv. Rev.* **2011**, *63*, 456–469. [[CrossRef](#)]
20. Menon, J.U.; Kona, S.; Wadajkar, A.S.; Desai, F.; Vadla, A.; Nguyen, K.T. Effects of surfactants on the properties of PLGA nanoparticles. *J. Biomed. Mater. Res. Part A* **2012**, *100*, 1998–2005. [[CrossRef](#)]
21. Della Sala, F.; Silvestri, T.; Borzacchiello, A.; Mayol, L.; Ambrosio, L.; Biondi, M. Hyaluronan-coated nanoparticles for active tumor targeting: Influence of polysaccharide molecular weight on cell uptake. *Colloids Surf. B Biointerfaces* **2022**, *210*, 112240. [[CrossRef](#)]
22. Cannavà, C.; De Gaetano, F.; Stancanelli, R.; Venuti, V.; Paladini, G.; Caridi, F.; Ghica, C.; Crupi, V.; Majolino, D.; Ferlazzo, G.; et al. Chitosan-Hyaluronan Nanoparticles for Vinblastine Sulfate Delivery: Characterization and Internalization Studies on K-562 Cells. *Pharmaceutics* **2022**, *14*, 942. [[CrossRef](#)] [[PubMed](#)]
23. Almalik, A.; Karimi, S.; Ouasti, S.; Donno, R.; Wandrey, C.; Day, P.J.; Tirelli, N. Hyaluronic acid (HA) presentation as a tool to modulate and control the receptor-mediated uptake of HA-coated nanoparticles. *Biomaterials* **2013**, *34*, 5369–5380. [[CrossRef](#)] [[PubMed](#)]
24. Gennari, A.; Rios de la Rosa, J.M.; Hohn, E.; Pelliccia, M.; Lallana, E.; Donno, R.; Tirella, A.; Tirelli, N. The different ways to chitosan/hyaluronic acid nanoparticles: Templated vs direct complexation. Influence of particle preparation on morphology, cell uptake and silencing efficiency. *Beilstein J. Nanotechnol.* **2019**, *10*, 2594–2608. [[CrossRef](#)]
25. Shipp, D.W.; Sinjab, F.; Notingher, I. Raman spectroscopy: Techniques and applications in the life sciences. *Adv. Opt. Photonics* **2017**, *9*, 315–428. [[CrossRef](#)]
26. Langer, J.; Jimenez de Aberasturi, D.; Aizpurua, J.; Alvarez-Puebla, R.A.; Auguie, B.; Baumberg, J.J.; Bazan, G.C.; Bell, S.E.; Boisen, A.; Brolo, A.G.; et al. Present and Future of Surface-Enhanced Raman Scattering. *ACS Nano* **2020**, *14*, 28–117. [[CrossRef](#)]
27. Lane, L.A.; Qian, X.; Nie, S. SERS Nanoparticles in Medicine: From Label-Free Detection to Spectroscopic Tagging. *Chem. Rev.* **2015**, *115*, 10489–10529. [[CrossRef](#)]
28. Zhou Rui, X.X.; Liu, R.; Hao, L.T.; Liu, J.F. Identification of polystyrene nanoplastics using surface enhanced Raman spectroscopy. *Talanta* **2021**, *221*, 121552. [[CrossRef](#)]
29. Xia, L.; Li, W.; Sun, M.; Wang, H. Application of SERS in the Detection of Fungi, Bacteria and Viruses. *Nanomaterials* **2022**, *12*, 3572. [[CrossRef](#)]
30. Isticato, R.; Sirec, T.; Giglio, R.; Baccigalupi, L.; Rusciano, G.; Pesce, G.; Zito, G.; Sasso, A.; De Felice, M.; Ricca, E. Flexibility of the programme of spore coat formation in *Bacillus subtilis*: bypass of CotE requirement by over-production of CotH. *PLoS ONE* **2013**, *8*, e74949. [[CrossRef](#)]
31. Rusciano, G.; Zito, G.; Isticato, R.; Sirec, T.; Ricca, E.; Bailo, E.; Sasso, A. Nanoscale chemical imaging of *Bacillus subtilis* spores by combining tip-enhanced Raman scattering and advanced statistical tools. *ACS Nano* **2014**, *8*, 12300–12309. [[CrossRef](#)]
32. Giarra, S.; Serri, C.; Russo, L.; Zepetelli, S.; De Rosa, G.; Borzacchiello, A.; Biondi, M.; Ambrosio, L.; Mayol, L. Spontaneous arrangement of a tumor targeting hyaluronic acid shell on irinotecan loaded PLGA nanoparticles. *Carbohydr. Polym.* **2016**, *140*, 400–407. [[CrossRef](#)] [[PubMed](#)]
33. Essendoubi, M.; Gobinet, C.; Reynaud, R.; Angiboust, J.F.; Manfait, M.; Piot, O. Human skin penetration of hyaluronic acid of different molecular weights as probed by Raman spectroscopy. *Skin Res. Technol.* **2016**, *22*, 55–62. [[CrossRef](#)]
34. Kotzianova, A.; Rebicek, J.; Zidek, O.; Pokorny, M.; Hrbac, J.; Velebny, V. Raman spectroscopy based method for the evaluation of compositional consistency of nanofibrous layers. *Anal. Methods* **2015**, *7*, 9900–9905. [[CrossRef](#)]
35. Barrett, T.W.; Peticolas, W.L. Laser Raman inelastic light scattering investigations of hyaluronic acid primary and secondary structure. *J. Raman Spectrosc.* **1979**, *8*, 35–38. [[CrossRef](#)]
36. Van Apeldoorn, A.A.; Van Manen, H.J.; Bezemer, J.M.; de Bruijn, J.D.; van Blitterswijk, C.A.; Otto, C. Raman imaging of PLGA microsphere degradation inside macrophages. *J. Am. Chem. Soc.* **2004**, *126*, 13226–13227. [[CrossRef](#)] [[PubMed](#)]
37. Geze, A.; Chourpa, I.; Boury, F.; Benoit, J.P.; Dubois, P. Direct qualitative and quantitative characterization of a radiosensitizer, 5-iodo-2'-deoxyuridine within biodegradable polymeric microspheres by FT-Raman spectroscopy. *Analyst* **1999**, *124*, 37–42. [[CrossRef](#)]
38. Guo, C.; Liu, H.; Wang, J.; Chen, J. Conformational Structure of Triblock Copolymers by FT-Raman and FTIR Spectroscopy. *J. Colloid Interface Sci.* **1999**, *209*, 368–373. [[CrossRef](#)]
39. Shaarani, S.; Hamid, S.S.; Mohd Kaus, N.H. The Influence of Pluronic F68 and F127 Nanocarrier on Physicochemical Properties, In vitro Release, and Antiproliferative Activity of Thymoquinone. *Drug Pharmacogn. Res.* **2017**, *9*, 12–20. [[CrossRef](#)]
40. Al-Milaji, K.N.; Zhao, H. New Perspective of mitigating the coffee-ring effect: Interfacial assembly. *J. Phys. Chem. C* **2019**, *123*, 12029–12041. [[CrossRef](#)]
41. Le Ru, E.C.; Meyer, S.A.; Artur, C.; Etchegoin, P.G.; Grand, J.; Lang, P.; Maurel, F. Experimental demonstration of surface selection rules for SERS on flat metallic surfaces. *ChemComm* **2011**, *47*, 3903–3905. [[CrossRef](#)]
42. Serri, C.; Argirò, M.; Piras, L.; Mita, D.G.; Saija, A.; Mita, L.; Forte, M.; Giarra, S.; Biondi, M.; Crispi, S.; et al. Nano-precipitated curcumin loaded particles: Effect of carrier size and drug complexation with (2-hydroxypropyl)- $\beta$ -cyclodextrin on their biological performances. *Int. J. Pharm.* **2017**, *520*, 21–28. [[CrossRef](#)]

43. Danaei, M.; Dehghankhold, M.; Ataei, S.; Hasanzadeh Davarani, F.; Javanmard, R.; Dokhani, A.; Khorasani, S.; Mozafari, M.R. Impact of particle size and polydispersity index on the clinical applications of lipidic nanocarrier systems. *Pharmaceutics* **2018**, *10*, 57. [[CrossRef](#)]
44. Honary, S.; Zahir, F. Effect of Zeta Potential on the Properties of Nano-Drug Delivery Systems—A Review (Part 1). *Trop. J. Pharm. Res.* **2013**, *12*, 255. [[CrossRef](#)]
45. Honary, S.; Zahir, F. Effect of Zeta Potential on the Properties of Nano-Drug Delivery Systems—A Review (Part 2). *Trop. J. Pharm. Res.* **2013**, *12*, 265. [[CrossRef](#)]
46. Capaccio, A.; Sasso, A.; Tarallo, O.; Rusciano, G. Coral-like plasmonic probes for tip-enhanced Raman spectroscopy. *Nanoscale* **2020**, *12*, 24376. [[CrossRef](#)]
47. Capaccio, A.; Sasso, A.; Rusciano, G. A simple and reliable approach for the fabrication of nanoporous silver patterns for surface-enhanced Raman spectroscopy applications. *Sci. Rep.* **2021**, *11*, 22295. [[CrossRef](#)]

**Disclaimer/Publisher's Note:** The statements, opinions and data contained in all publications are solely those of the individual author(s) and contributor(s) and not of MDPI and/or the editor(s). MDPI and/or the editor(s) disclaim responsibility for any injury to people or property resulting from any ideas, methods, instructions or products referred to in the content.